Chromodynamic Lattice Boltzmann Method for the Simulation of Drops, Erythrocytes, and other Vesicles

J. Spendlove[1,2], X. Xu[1,2], T. Schenkel[1,2], J. P. Gunn[3] and I. Halliday[3,*]

[1] *Department of Engineering and Mathematics, Sheffield Hallam University, Howard Street, S1 1WB, UK.*
[2] *Materials & Engineering Research Institute, Sheffield Hallam University, Howard Street, S1 1WB, UK.*
[3] *Department of Infection, Immunity and Cardiovascular Disease, The Medical School, Beech Hill Road, Sheffield, S10 2RX, UK.*

Abstract. Recently, we have validated a three-dimensional, single framework multi-component lattice Boltzmann method, modified to generate vesicles (rather than drops) ["Three-dimensional single framework multicomponent lattice Boltzmann equation method for vesicle hydrodynamics," Phys. Fluids 33, 077110 (2021)]. This approach implements an immersed boundary force distribution, characterised by bending rigidity, surface tension, preferred curvature and conserved membrane area, in which work we successfully validated isolated vesicle flows against other methodologies and experiment. Like most immersed boundary algorithms, our method relies on numerical computation of high-order spatial derivatives and an intricate body force density. The next step is to verify that it has sufficient numerical stability to address the anticipated application of high volume fraction flows of highly deformable objects in intimate interaction. It is this *in silico* verification – of both the class of fluid object attainable and the stability of the later in strong, straining and shearing flows which is at issue, here. We extend our method to simulate multiple variously deflated vesicles and multiple liquid droplets still within a single framework, from which our fluid objects emerge as particular parameterisations. We present data from simulations containing up to four vesicles (five immiscible fluid species), which threshold verifies that simulations containing unlimited fluid objects are possible ["Modeling the flow of dense suspensions of deformable particles in three dimensions," Phys. Rev. E 75, 066707 (2007)]. These

Corresponding author. Email addresses: `i.halliday@sheffield.ac.uk` (I. Halliday), `James.Spendlove@student.shu.ac.uk` (J. Spendlove), `xu.xu@shu.ac.uk` (X. Xu), `T.Schenkel@shu.ac.uk` (T. Schenkel), `j.gunn@sheffield.ac.uk` (J. P. Gunn)

data also assure the ability of our immersed boundary forcing to preserve the character and integrity of fluid objects in interactions characterised by large local velocity gradients (intimate squeezing, shearing and elongational straining). Throughout, we take interfacial or membrane area, A, as a proxy for stability and physical veracity.

---

1 Introduction

Advances in novel computational fluid dynamics (CFD) methodology hold-out the meaningful prospect of complex, three-dimensional time-dependent simulations of fluid objects, such as vesicles, cells and other suspended, neutrally buoyant entities, which deform when they advect, i.e., exhibit intimate coupling to any motion of the embedding, or background fluid. Of course, the complexity of what we designate fluid objects is variable, spanning for example:

- Deflated vesicles (i.e., erythrocytes), which have locally inextensible membranes, with bending rigidity, surface tension and, not least, a significant excess of conserved membrane area.

- Capsules, which contain in-plane shear elasticity (beyond the scope of the present work, but also have extensible interfaces with embedding fluid [1]).

- Drops, being the simplest fluid object, having an extensible interface governed only by interfacial tension.

A common feature of these objects is that all are filled with incompressible fluid, of a density similar to that of the embedding, background fluid. Furthermore, the interface or membrane is regarded as discontinuous (i.e., very narrow), when the fluid object is treated within the continuum regime of fluid mechanics [2].

The rheology of a wide range of complex fluids, defined as having emergent properties which rest upon their composition at the micron scale (which still lies within the continuum regime, of fluid dynamics, note) is of central importance in physiology, biomedicine, chemical engineering, food rheology, material science and bio-engineering applications *inter alia*. The simulation of liquid drops has high importance, e.g., in the emerging study of liquid drops' impact upon and wetting of the elastic surfaces of new materials [3]. Other fluid objects with small deflation and conserved membrane area widely serve as cell proxies and are frequently found in food processing and pharmacological flows [4]. Finally, the simulation of vesicles being of unquestionable importance

in pharmacology and applied physiology (e.g., in establishing the principles of micro-vascular resistance). The work presented here is aimed at the further computational verification of an accessible, lattice Boltzmann method (LBM) based tool, for investigating the emergent rheology of dense suspensions of a wide class of fluid object.

It is appropriate to identify alternative approaches to this problem and differentiate our own, at the outset, emphasizing LBM-based approaches. LBM, an increasingly mainstream mesoscale fluid dynamics technique which indirectly solves the continuum Navier-Stokes equations, has been applied to a wide range of multicomponent flow. The technique has been variously enhanced to simulate multiple phases, components and, hence, complex fluid objects. The fluid-structure interaction process in LBM is, perhaps, its essential feature. Approaches to the simulation of flow containing multiple fluid objects, i.e., erythrocytes, can be conveniently classified as: (i) single-framework; or (ii) modular, multi-framework. We classify approaches by the number of techniques needed to resolve the simulation: single-framework being a single technique and multi-framework being based on multiple techniques. Advantages of the former are transparency of physical content combined with implementational and computational simplicity- they offer direct control of resolution, parameterisation and are implemented within a single computer code platform.

Multi-framework approaches use distinct techniques, typically, LBM solvers for the fluid domain, a separate finite element method (FEM) for the membrane dynamics, and some means pairing them. The FEM-LBM approach achieved simulations containing $\mathcal{O}(10^3)$ objects more than a decade ago [5, 6]. It employs Lagrangian markers on the membrane surface (which are not co-registered with the LBM mesh, note) which are two-way coupled to the fluid solver, via a membrane force distribution (the latter is interpolated onto the local Eulerian nodes of the LBM fluid solver). The advantages of such an approach are: (i) all mechanical properties are directly assigned; (ii) developmental maturity; and (iii) portability (the fluid solver is readily interchangeable). An example of this essential approach is the simulation by Krüger [7], of erythrocytes, in which the governing dynamics of the membrane material are discretised, using finite element method (FEM), then coupled to the LBM fluid solver via the immersed boundary method (IBM) [8, 9]. A further relevant example is Hemocell, which uses discrete-element method and the IBM to resolve and couple the cellular membranes with an LBM fluid solver [10,11]. Applications of this multi-framework tool typically require grid-scale computing resource, note, and specifically target hemodynamics. Furthermore, there are a variety of other FEM-LBM models for such applications [7, 12]. In addition, the FEM-LBM approach has been applied to the simulation of soft particles [13].

In contrast to these established, multi-framework approaches, we recently presented a complementary, single-framework, chromodynamic multi-component lattice Boltzmann method (cMCLBM), adapted to vesicle hydrodynamics (specifically RBCs), the scope of which we extend here. We have addressed verification of physical content, based upon steady state and dynamical data on single RBC deformation [14]. The model was shown to be a promising tool, practically and theoretically, its foundations (kinematics and dy-

namics) being carefully constructed from prior art [15–17]. Its intended advantages are: (i) a single framework foundation within cMCLBM, carrying an automatic two-way coupled fluid-structure interaction; and (ii) mathematical transparency of physical content. The method also has some indirect advantages as follows; it contains an automatically adaptive interface, with no re-meshing issues (even in the most intimate interactions, as our data here demonstrate), it has strict mass conservation, it is robust and stable far from mechanical equilibrium, it is amenable to parallelisation and, not least, it inherits an ability to scale efficiently to many fluid objects, using previously developed methodologies [18] (which is also of concern here). Here, then, we extend our prior work by pursuing two key aims:

– To outline an extension to cMCLBM [14], which facilitates the simulation of multiple, immiscible fluid objects of variable character, as mutually immiscible fluid components

– To verify this single-framework, enhanced cMCLBM for multiple fluid objects, to verify that suspensions of liquid drops, erythrocytes, and other vesicles then fall within the scope of the method.

Our second objective amounts to an address of the following question. Is the dynamics of fluid objects, which previous work has validated (in isolation) [14], stable when such objects encounter each other, in the presence of very high fluid object deformation, local fluid strain rates and confinement effects? Our position is that this and a range of other validations are inherited when the validated diphasic method is extended to multiple immiscible fluids —because any two fluid pairs will behave as if they are diphasic. We argue that validation then reduces to a myopic examination of the triple and quadruple contacts (which matter has been addressed, in the past). In the envisaged applications to suspensions, such contacts are very rare indeed. The next, truly significant step in the workflow is therefore to verify the stability of a range of multiple objects in intimate interaction —which is what we aim to address here. Put another way, we would argue that extended validation must focus on the intimate behaviour of complex contacts (whose stability we do address, note) for which no theory known to us exists – other than lubrication theory, of course.

We proceed as follows. Section 2 presents an enhanced, single-framework cMCLBM, after Burgin et al., [14,15] incorporating extensions into our approach, specifically a compartmentalised immersed force system to target particular behaviours and an extension to many immiscible fluids. In Section 3, tests demonstrating the model's ability to simulate multiple fluid objects, as well as its stability and robustness are presented. Simple tests will employ geometries which encourage strong shear and squeeze motion in the contact region, in presence of external confinement and will also showcase the advantages of our single-framework methodology's automatic interface tracking in the context of heavily strained fluid objects. In Section 4, conclusions will be presented. For the sake of completeness, we present an important, putative extension to our core cMCLBE

methodology within Appendix. A, which has the potential to reduce algorithmic complexity and reduce computational expense when scaling to many fluid object flows.

2 Methodology

We present an abbreviated account of single framework cMCLBM, emphasising the role of the immersed boundary force distribution. The latter dictates the physics of the fluid object. To address the simulation of liquid drops (superscript D), erythrocytes (superscript E) and spherical vesicles (superscript SV), it is convenient to postulate three immersed boundary force contributions: (a) $\underline{F}^{(D)}$, (b) $\underline{F}^{(E)}$ and (c) $\underline{F}^{(SV)}$. Throughout, notation is chosen to align with that traditionally used within the LB community- see e.g. [14, 15].

2.1 Chromodynamic MCLBM

LBM is a bottom-up Eulerian approach, in which the probability distribution function for a fluid parcel is evolved on a discrete lattice. The method works at the length-scale of a minimal form of kinetic theory and is constructed to recover the continuum Navier-Stokes equations. The historic foundations of our variant trace back to 1991, in the work of Gunstensen et al., [19, 20] and Latva-Kokko and Rothman [21], which extended the prior Rothman-Keller lattice gas model [22]. From this work, distinct multi-component (MC) and multi-phase (MP) lattice Boltzmann method (LBM) variants have been developed. For more information on these variants, see the following [14, 15, 23–27]. In this work, we utilise Spendlove's cMCLBM diphasic variant [14], for isolated RBCs, here extending, then verify this methodology, to reach multiple immiscible fluid objects. For tractability and simplicity however, the key extensions of the methodology, necessary to reach multiple immiscible fluids are presented in the context of two component flow.

Consider three-dimensional two-fluid simulation, using a multi-relaxation time (MRT) scheme, on the $D3Q19$ lattice; see Table 1 for lattice Cartesian velocity vectors $\underline{c}_i$, our link label convention $i \in 0, 1, \cdots, 18$ and the two associated link weight sets (denoted ω_i and g_i [28]).

For a binary fluid, identify the internal (external) fluid by a color label: Red (Blue). The net fluid parcel distribution function is a sum of the contributions of the fluid species [15, 19]:

$$f_i(\underline{r}, t) = R_i(\underline{r}, t) + B_i(\underline{r}, t), \tag{2.1}$$

where the forced evolution equation of the parcel distribution function is:

$$f_i(\underline{r} + \underline{c}_i \Delta t, t + \Delta t) = f_i(\underline{r}, t) - \sum_{j=0}^{Q-1} \Omega_{ij}(f_j(\underline{r}, t) - f_j^{(0)}(\rho, \underline{u})) + F_i. \tag{2.2}$$

Table 1: $D3Q19$ lattice structure, showing lattice link (i), lattice velocity vector ($\underline{c}_i$) components and lattice weights (ω_i, g_i). Here, $\omega_0 = \frac{1}{3}$, $\omega_1 = \frac{1}{18}$, $\omega_2 = \frac{1}{36}$ and $g_0 = 1$, $g_1 = -2$, $g_2 = 1$.

i	0	1	2	3	4	5	6	7	8	9	10	11	12	13	14	15	16	17	18
c_{ix}	0	1	1	0	-1	-1	-1	0	1	0	1	0	-1	0	0	1	0	-1	0
c_{iy}	0	0	-1	-1	-1	0	1	1	1	0	0	1	0	-1	0	0	1	0	-1
c_{iz}	0	0	0	0	0	0	0	0	0	1	1	1	1	1	-1	-1	-1	-1	-1
ω_i	ω_0	ω_1	ω_2	ω_1	ω_2	ω_1	ω_2	ω_1	ω_2	ω_1	ω_2	ω_2	ω_2	ω_2	ω_1	ω_2	ω_2	ω_2	ω_2
g_i	g_0	g_1	g_2	g_1	g_2	g_1	g_2	g_1	g_2	g_1	g_2	g_2	g_2	g_2	g_1	g_2	g_2	g_2	g_2

Xu et al. [29] give the MRT collision matrix, $\underline{\underline{\Omega}}$. The equilibrium distribution function ($f_i^{(0)}$) and our source term (F_i), are [30]:

$$f_i^{(0)}(\rho,\underline{u}) = \omega_i \rho \left(1 + \frac{u_\alpha c_{i\alpha}}{c_s^2} + \frac{u_\alpha u_\beta c_{i\alpha} c_{i\beta}}{2c_s^4} - \frac{u^2}{2c_s^2} \right), \tag{2.3}$$

$$F_i = \omega_i \left[\frac{\underline{F}^{(T)} \cdot c_{i\alpha}}{c_s^2} + \frac{1}{2c_s^4} \left(1 - \frac{\lambda_3}{2} \right) \left(F_\alpha^{(T)} u_\beta + F_\beta^{(T)} u_\alpha \right) \right]. \tag{2.4}$$

Above, $\underline{r}$, t, Δt, ρ, $\underline{u}$, Q, $F^{(T)}$, c_s and λ_p denote lattice position, lattice time, time step, macroscopic fluid density, macroscopic fluid velocity, number of lattice links, total immersed body force, color-blind speed of sound, and the pth eigenvalue corresponding to the collision matrix Ω_{ij}, respectively. Greek subscripts identify Cartesian components. To recover correct bulk hydrodynamics, the source term must meet the following conditions (see Guo et al. [30]):

$$\sum_i (1, \underline{c}_i, \underline{c}_i \underline{c}_i) F_i = \left(0, n\underline{F}^{(T)}, \frac{1}{2}[\underline{C} + \underline{C}^{\mathsf{T}}] \right), \tag{2.5}$$

where $\underline{C}$ ($\underline{C}^{\mathsf{T}}$) is a correction term (correction term transposed), needed to recover the Navier-Stokes equations [30, 31]. The MRT scheme collision matrix $\underline{\underline{\Omega}}$ is described in reference [29] and is conceived after that of Dellar [32]; it must also have certain properties:

$$\sum_i (\underline{c}_i, \underline{c}_i \underline{c}_i, \underline{c}_i \underline{c}_i \underline{c}_i) \Omega_{ij} = \left(0, \lambda_4 c_{j\alpha} c_{j\beta}, \lambda_{14} c_{j\alpha} c_{j\beta}^2 \right), \tag{2.6}$$

$$\sum_i (g_i, g_i \underline{c}_i, g_i \underline{c}_i \underline{c}_i) \Omega_{ij} = \left(\lambda_{10} g_j, \lambda_{11} g_j c_{j\alpha}, \lambda_{17} g_j c_{j\alpha}^2 \right). \tag{2.7}$$

To compute local, continuum properties (density and velocity), the force-corrected moments are used [30, 33]:

$$(\rho_R, \rho_B) = \sum_i (R_i, B_i), \quad \underline{u} = \frac{\sum_i f_i(\underline{r}, t) \underline{c}_i}{\rho} + \frac{\underline{F}^{(T)}}{2\rho}, \tag{2.8}$$

where ρ_R (ρ_B) is the Red (Blue) fluid density (nodal density is computed straightforwardly as $\rho = (\rho_R + \rho_B)$). The flow velocity is adjusted, using the immersed boundary force $F^{(T)}$, note. We shall return to this matter later.

A chromodynamic field is constructed from the distribution of the color degree of freedom (see [34]):

$$\rho^N(\underline{r},t) \equiv \frac{\rho_R(\underline{r},t) - \rho_B(\underline{r},t)}{\rho_R(\underline{r},t) + \rho_B(\underline{r},t)} \in [-1,1]. \tag{2.9}$$

$\rho^N = 1$ (-1) corresponds to bulk Red (Blue) components, $\rho^N = 0$ corresponds to the centre of the interface, taken here as the effective surface. From this definition, the local interface unit normal is straightforwardly assigned as below:

$$\hat{n}(\underline{r},t) = -\frac{\nabla \rho^N(\underline{r},t)}{|\nabla \rho^N(\underline{r},t)|}. \tag{2.10}$$

The above quantity is utilised to calculate the surface curvatures, required by the immersed force $F^{(T)}$ (see reference [14]).

To prevent mixing, a kinetic-scale, post-collision, color segregation rule, adapted from that of d'Ortona et al., [35] is used:

$$C_i^{\psi\psi}(\underline{r},t) = \frac{\rho_C(\underline{r},t)}{\rho(\underline{r},t)} f_i(\underline{r},t)^\psi \pm \beta \omega_i \frac{\rho_R(\underline{r},t)\rho_B(\underline{r},t)}{\rho(\underline{r},t)} \hat{n} \cdot \underline{c}_i \Delta t. \tag{2.11}$$

Here, C is the color index $C \in [R,B]$ where operation $+$ ($-$) is used for the Red (Blue) fluid. Superscript $\psi\psi$ (ψ) denotes the post-recolor (post-collision) value. We return to discuss the interfacial width (or segregation parameter), β, below.

The immersed boundary force to be used in Eqs. (2.4, 2.8) carries the interaction between the fluid and the embedded object. It is a gradient-weighted vector ($\nabla \rho^N$ lies in the surface normal direction). Force $\underline{F}^{(T)}$, by construction, encapsulates the continuum scale physics of the boundary of the object being simulated:

$$\underline{F}^{(T)} = \frac{1}{2} \nabla \rho^N \left(F^{(\chi)} \right), \quad \chi \in \{D,E,SV\}. \tag{2.12}$$

Above, superscripts D, E, SV denote drops, erythrocytes and spherical vesicles, respectively.

Modular immersed forces

As we consider three classes of object, for each there exists an appropriate immersed boundary fluid body force. For each of the three cases, we consider:

$$\text{(Drops)} \qquad\qquad \underline{F}^{(D)} = \underline{F}^{(l)}, \tag{2.13}$$

$$\text{(Erythrocytes)} \qquad \underline{F}^{(E)} = \underline{F}^{(a)} + \underline{F}^{(b)} + \underline{F}^{(l)}, \tag{2.14}$$

$$\text{(Spherical Vesicles)} \quad \underline{F}^{(SV)} = \underline{F}^{(a)} + \underline{F}^{(b)} + \underline{F}^{(l)}, \tag{2.15}$$

where $\underline{F}^{(a)}$, $\underline{F}^{(b)}$ and $\underline{F}^{(l)}$ are the area conserving, the bending and the surface tension forces, respectively. Of course, in addition to force structure, parameterisation dictates the physics of the emergent fluid objects. We will return to this matter in Section 3.

The surface tension force ($\underline{F}^{(l)}$) reflects differential forces operating between molecules of similar and mutually immiscible (we use the term "opposing") components. Surface tension effects emerge, within cMCLBM, from the application of the Lishchuk force [34]:

$$\underline{F}^{(l)} = 2\sigma H \hat{n}, \tag{2.16}$$

where σ is the surface tension parameter and H the mean interface curvature.

Area force, ($\underline{F}^{(a)}$), which conserves the area of the membrane or interface, close to a target value A_0 is:

$$\underline{F}^{(a)} = -\alpha H (A - A_0) A \hat{n}, \tag{2.17}$$

where α, A and A_0 denote interface compressibility, actual area and target membrane or interface area.

Bending force ($\underline{F}^{(b)}$) communicates membrane or interface bending rigidity energy effects into the interface fluid. Our bending rigidity force derives from Helfrich's bending energy [36,37], which follows Helrich's proposal that by treating the membrane as a two-dimensional sheet (based on the separation of length scales), the bending deformations of this sheet play a key role in the membrane elasticity, and hence the shape of the erythrocyte [38]. As such, this force is used to determine the shape of the boundary between the internal and external fluid at all times when simulating vesicles, and is given in the form described in [14]:

$$\underline{F}^{(b)} = -\kappa_B \left(\frac{3}{2} \Delta_S H + H^3 - KH \right) \hat{n}. \tag{2.18}$$

Above, κ_B, Δ_S and K represent the bending rigidity constant, the Laplace-Beltrami operator and the Gaussian curvature of the interface (i.e., the membrane surface), respectively. Note, Eqs. (2.16), (2.17), (2.18) all depend upon H and K. Efficient methodologies for computing them (and Δ_S) solely from the instantaneous interface unit normal field, $\hat{n}(\underline{r}, t)$, were devised in reference [14]. We remark that the surface curvature (and hence deflation) of an erythrocyte membrane is controlled in part by the cytoskeleton and in part by the properties of the encapsulating lipid bi-layer. Clearly, $\underline{F}^{(b)}$ is a meso-scale representation of the membrane which aggregates all effects on surface curvature.

2.2 Extension to many immiscible fluid objects

Section 2.1 considers binary lattice fluids. However, the binary method is readily extendable to many, mutually immiscible components and fluid objects. We remark the rate of evolution of cMCLBM methodology in this direction is accelerating [18, 39–41], presumably, because cMCLBE offers strict species mass conservation and tuneable surface tensions. Here we consider physics of three-component liquid-liquid contacts only, so it
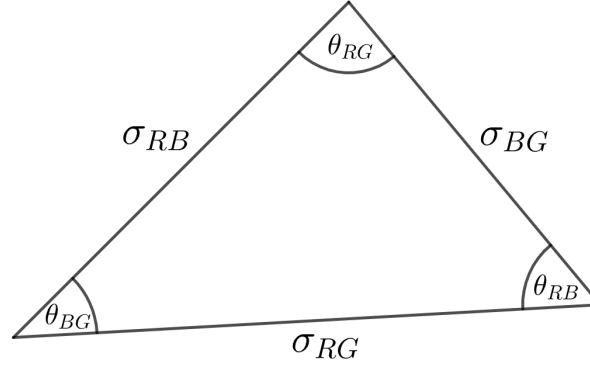
Figure 1: A representation of the forces at triple contact between three, mutually immiscible fluids, here denoted Red (R), Blue (B) and Green (G) which are in mechanical equilibrium. The surface tensions between the fluid pairs are denoted $\sigma_{CC'}$ and the contact angles by $\theta_{CC'}$, where $C, C' \in [R, B, G]$, with $C \neq C'$.

is upon the physics of wetting alone that we base our control of fluids' mutual immiscibility. Put another way, for tractability we neglect, e.g., bending force effects in our approach to controlling the integrity of fluid objects. This assumption may only be justified *a posteriori*.

The relevant continuum-scale fluid mechanics of a three-phase contact is encapsulated in Neumann's triangle, which, at a contact, relates the surface tensions forces between three interacting fluids [42, 43]. For a triple contact, assigning individual surface tension values for each fluid interface establishes the contact geometry illustrated in Fig. 1.

Mutually immiscible, wetting fluids must produce a triple contact geometry consistent with the Young-Laplace law and Neumann's triangle. Unfortunately, in cMCLBM, assigning differentiated surface tension values for which no stable contact exists does not necessarily underwrite compliance with the Young-Laplace law. This is due to the method's inherent dispersion and the pathological finite width of its continuum interface. Consequently, one cannot simply parameterise interfacial tension so as to preclude contact formation- further methodological enhancements are necessary. The cMCLBE segregation rule has been enhanced to treat triple contacts [18,39,41], most recently by Yu et al., [41], who define a form which successfully approximates physical three-component behaviour. Here, once correct contact geometry is enforced, no explicit hydrodynamic repulsion is postulated into the method; put another way, causal lubrication forces emerge. This contact behaviour is of course fully consistent with lubrication theory, which is implicit within any method which solves the Navier-Stokes equations. We adopt and contextualise their process, now with a form of Eq. (2.11), extended to the simulation of three components [18]:

$$C_i^{\psi\psi} = \frac{\rho_C}{\rho} f_i^{\psi} \pm \omega_i \Delta t \underline{c}_i \cdot \left(\sum_{C'} \beta_{CC'} \frac{\rho_C \rho_{C'}}{\rho} \hat{n}_{CC'} \right).$$

The cMCLBE segregation parameter (effective interface width) between fluids C and C' is controlled by $\beta_{CC'}$, but in the case of a triple contact, also by the surface tension values themselves. For triple contact behaviour, then, appropriate values of $\beta_{CC'}$ are calculated using the cosine rule in the form by Eq. (2.19a) (see also Fig. (1)), then, using this value to determine how the interface width between fluids C and C' should be perturbed. This process gives correct wettability between the fluids, in the form of Eqs. (2.19b,2.19c), [41]:

$$X_{CC'} = \frac{\sigma_{C''C}^2 + \sigma_{C''C'}^2 - \sigma_{CC'}^2}{2\sigma_{C''C}\sigma_{C''C'}}, \tag{2.19a}$$

$$\beta_{CC'} = \beta^0 + \beta^0 \min\left(\frac{35\rho_C\rho_{C'}\rho_{C''}}{\rho^3}, 1\right) g(X_{CC'}), \tag{2.19b}$$

$$g(X_{CC'}) = \begin{cases} 1, & X_{CC'} < -1, \\ 1 - \sin(\arccos(X_{CC'})), & -1 \leq X_{CC'} < 0, \\ \sin(\arccos(X_{CC'})) - 1, & 0 \leq X_{CC'} < 1, \\ -1, & X_{CC'} < 1. \end{cases} \tag{2.19c}$$

Above, component indices $C \neq C' \neq C''$ represent the three separate fluids, and $\beta^0 = 0.6$ was used for all simulations in this work.

We consider completely immiscible fluid objects, here. Accordingly, segregation must maintain complete immiscibility between all fluid pairs, i.e., no stable Neumann's triangle geometry must be permitted. Suppose fluid objects are not initialised overlapping each other; the surface relative tension of the fluid object O to background fluid B being $\sigma_{OB} = \sigma_0$. Then by ensuring the surface tension between two fluid objects, O and O', is such that $\sigma_{OO'} \geq 2\sigma_0$, the fluids should remain immiscible. Under these assumptions, the equations developed in [41] can be simplified. Now the interface width parameter values for a given object-background OB and object-object pairing OO' are chosen as:

$$\beta_{OB} = \beta^0 - \beta^0 \min\left(\frac{35\rho_O\rho_B\rho_C}{\rho^3}, 1\right), \tag{2.20a}$$

$$\beta_{OO'} = \beta^0 + \beta^0 \min\left(\frac{35\rho_O\rho_{O'}\rho_C}{\rho^3}, 1\right), \tag{2.20b}$$

where subscripts B, O, O', C denote background fluid, a given fluid object, a different fluid object, and the component with largest density at a given lattice site excepting O, O', respectively. Eqs. (2.20a), (2.20b) now represent the revised perturbations needed to control the interface widths between fluid pairs. This device, (and setting the surface tension value of an object-object interface to twice that of an object-background interface) supports many mutually immiscible objects. We remark that the computational cost of these steps is significant. Currently, interfaces between possible pairs of fluids are defined; hence the number of binary interfaces dramatically increases with the number of fluids as:

$$\text{No. of interfaces} = \frac{n(n-1)}{2}. \tag{2.21}$$

The storage required increases quickly with the number of fluids, as well as the direct computational time (there is a need to loop over more interface pairs, performing expensive calculations of color fields, unit normals, and segregation allocations steps). To address this, we propose a re-defined color-field, defined between fluid components and the totality of its complement, a derivation of which is given in Appendix A. This simplification reduces the number of interfaces to parity with the number of individual fluids, i.e., fluid objects. An interface between a given fluid and all the remaining fluids, regarded as a single effective species is, of course, valid only within the context of forbidden triple contacts. However, a simplified color-field, generating only a single segregation term for each nodal fluid must dramatically decrease computational complexity and lead to fewer frequently executed, nested computational loops. Note that scheme in Appendix A is not used in the present work.

3 Results

We created squeeze and shear contact flows for each of the three classes of fluid object, to generate very high deformations, for fluid objects in close proximity. The tests reported below should be viewed as limiting cases, designed to probe and verify the computational stability of our method. The fact that such interactions are unlikely in practice is therefore beside the point. A positive outcome is that our data tend to verify that the physical character of fluid objects is preserved in the combined presence of high deformation, close proximity of other, equivalent, objects and large spatial velocity gradients in the contact region. The simplest and most measurable proxy for physical character, in the current context, is the area of interface/membrane of the fluid object, with the background fluid, A. A must be conserved for all classes of vesicles, at all stages of any interaction (in contradistinction, A can vary dramatically for drops in equivalent circumstances). Note, all the color maps within this work correspond to the surface area of the fluid objects.

3.1 Liquid drops, erythrocytes and spherical vesicles

We test three different classes of fluid objects: liquid drops (D), erythrocytes (E) and spherical vesicles (SV) and characterise them as follows:

– Mutually immiscible liquid drops' interface behaviour is governed by surface tension forces alone. They have an initial area $A = A_{\mathrm{sphere}}$, which is not conserved.

– Erythrocytes are fluid-filled vesicles, with interface properties governed by surface tension, area conserving and bending rigidity forces. They have an initial membrane area $A = Y A_{\mathrm{sphere}}$ which is conserved and we restrict our attention to a bicuspid shape, by regulating the deflation. In this work, Y is a deflation parameter, controlling the surface area to volume ratio [14].
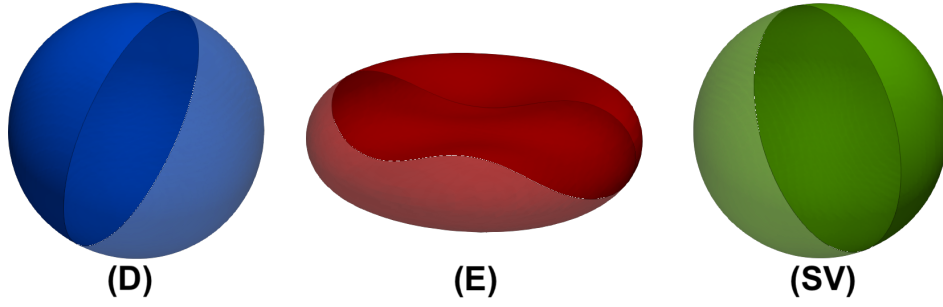
Figure 2: Schematic of the color and naming convention used for the three fluid objects simulated in this work. Drops are denoted D, erythrocytes E and spherical vesicles SV. Drops are depicted in blue, erythrocytes in red and spherical vesicles in green. Vesicles have a regulated surface area, drops do not. For cMCLBE parameterisations from which these fluid objects emerge (for a given lattice resolution and initial fluid object radius) see Table 2. See also [14].

Table 2: Parameterisations for the fluid objects simulated in this work, all expressed in lattice units. Force density amplitude constants are stated in lattice units and applied to a fluid object initialised with spherical shape, with an initial radius of 15 lattice units.

	Deflation, Y	Bending rigidity, κ_B	Surface tension, σ
Drops	NA	NA	10^{-3}
Erythrocytes	1.31	1.5	10^{-4}
Spherical vesicle	1.0	10^{-5}	10^{-3}

  – Spherical vesicles are also treated as vesicles with a reduced deflation – set to unity, here.

These three different fluid objects are represented schematically in Fig. 2 and a parameterisation, established based of prior work [14], is given in Table 2. For the fluid objects, an initial resolution of fluid object radius R= 15 is applied following prior work by the authors which checked grid independence, and deemed this resolution to be an appropriate option for balancing both accuracy and computational expense [14]. The area force parameter, α, is excluded from this tabulation because its value needs only to exceed a threshold. Accordingly, the emergent fluid object is determined by the parameter vector (Y, κ_B, σ) The color depiction in Fig. 2 is utilised throughout this article.

3.2   Pseudo-ballistic fluid object interactions

By using buoyancy forces and appropriate initial fluid object locations, we will propel the fluid objects towards each other. The resulting orbits and concurrent deformations will bring the objects into close proximity, but not into contact, due to the action of lubrication forces. We designate these processes pseudo ballistic. We stress that no physical forces other than buoyancy forces and the required immersed boundary forces already described are applied between the fluid objects in any of the tests reported here. Ap-
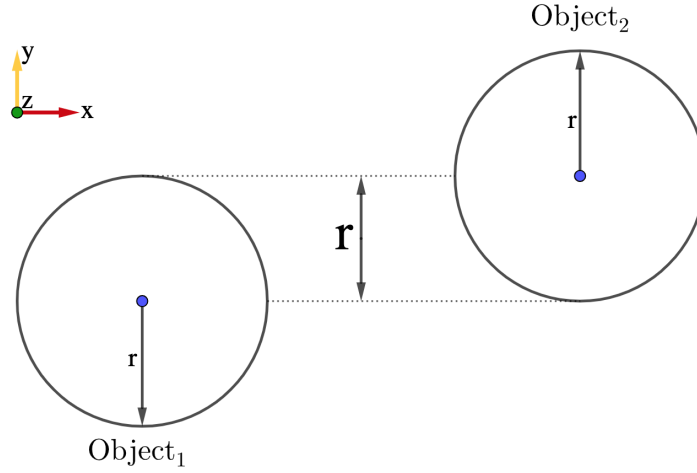
Figure 3: The initialisation of a pseudo-ballistic impact test for two equivalent fluid objects. Two fluid objects are to be buoyancy-forced parallel to the x direction, their centres being offset by an impact parameter r, equal in value to the objects' initial radius. Following initialisation, Object$_1$ (Object$_2$) is accelerated by application of a buoyancy force in the positive (negative) x-direction.

parent hydrodynamic repulsion effects emerge from fluid conservation and lubrication effects. Of course Van der Waals forces and other electrostatic effects can be postulated into our approach, if required.

As an initial test of the revised segregation rule (Section 2) and our cMCLBE methodology, we consider pseudo-ballistic impacts of multiple drops, erythrocytes and spherical vesicles. These tests verify: (i) the extended segregation rule, (ii) simulation stability and (iii) fluid objects' integrity. We consider two fluid objects in Section 3.2.1 and three fluid objects in Section 3.2.2. The motion of the background fluid in the contact region is best characterised as a shear flow.

3.2.1 Two fluid objects

All data presented correspond to a cuboid simulation box size $160 \times 100 \times 100$ on a D3Q19 lattice with periodic boundary conditions enforced between all faces. We initialise the objects such that there is no common interface between them, with their axes of rotation parallel. The test geometry is depicted in Fig. 3. The fluid objects are propelled towards each other by buoyancy forces, impressed parallel and anti-parallel to the x-axis, causing them to interact: Object$_1$ (Object$_2$) is pushed in the positive (negative) x-direction.

Figs. 4 show six sequential time frame snapshots indexed (A)-(F), from a pseudo-ballistic impact orbit of two: liquid drops (a); erythrocytes (b); and spherical vesicles (c). Fluid objects' surfaces were taken at the level set $\rho^N = 0$ (the centre of the fluid interface). The color intensity in the figures shows the surface area of the fluid objects. In all simulations, for these data, the applied buoyancy force for fluid Object$_1$ (Object$_2$) was $G = 1 \times 10^{-4} \hat{e}_x$ ($G = -1 \times 10^{-4} \hat{e}_x$) lattice units. The data from Figs. 4, show that the fluid objects partially orbit around each other, presumably due to hydrodynamic repul-

(a) Drops. 0, 4500, 7000, 8250, 9500 and 10500 time steps.

(b) Erythrocytes. 0, 1800, 2700, 3600, 4200 and 4800 time steps.

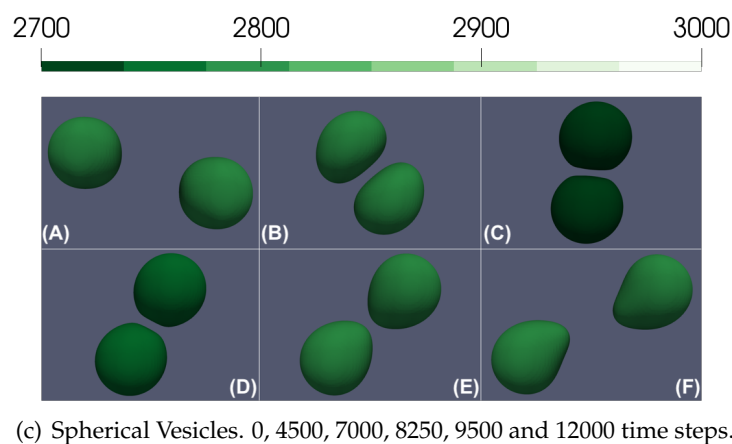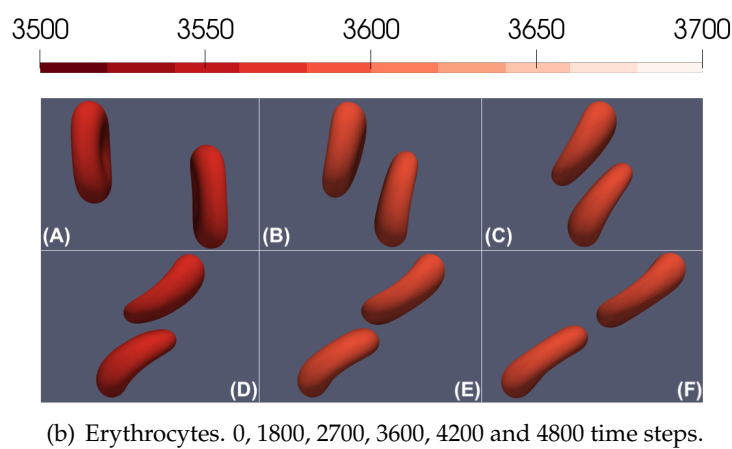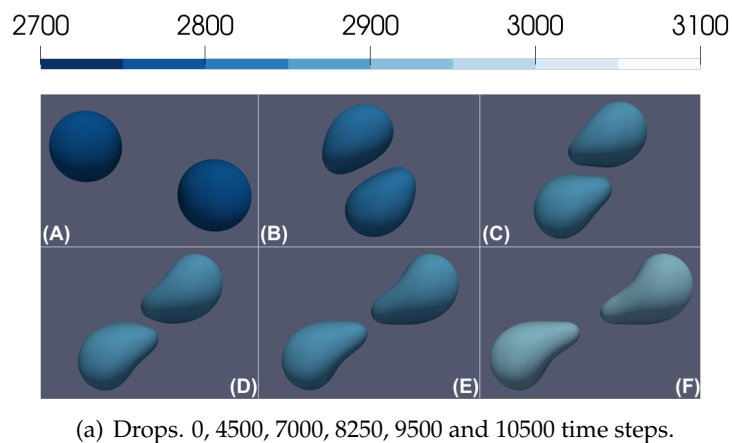(c) Spherical Vesicles. 0, 4500, 7000, 8250, 9500 and 12000 time steps.

Figure 4: A two fluid object pseudo-ballistic impact experiment, with sub-figures (a), (b), (c), corresponding to drops, erythrocytes and spherical vesicles, respectively. Here, the objects were pushed in the positive (negative) x-direction, causing them to interact. Time evolution is ordered as (A)-(F) at increasing times steps (given in sub-figure captions). The simulation view is from the positive z-axis (x–y plane) (see Fig. 3 for axis orientation).

Table 3: The maximum change in surface area during two-object pseudo-ballistic impact tests for the liquid drops, erythrocyte and spherical vesicle orbits depicted in Figs. 4. We record the initial area of the fluid object, before the force was applied, the maximum deviation of fluid object surface area, and the relative maximum surface area deviation throughout the simulation.

	Initial Area	Max Deviation	Max Relative Deviation %
Drops	2768	2917	5.4
Erythrocytes	3575	3581	0.2
Spherical Vesicle	2776	2718	2.0

sion (i.e., lubrication effects) which is expected to emerge, within the single framework methodology. This behaviour would not manifest, were the segregation stage outlined in Section 2, not enforcing complete immiscibility. Our liquid drops' interface surface area fluctuates by a maximum of $\approx 5.4\%$. In contradistinction, for the erythrocyte and spherical vesicle simulations, there is a maximal fluctuation in surface area $\approx 0.2\%$ and $\approx 2.0\%$, respectively. See Table 3. The latter result is, of course, expected – both the erythrocyte and spherical vesicle resist change in surface area due to their more complex membranes, providing further conformation of the effectiveness of the area conserving force outlined in [14], and given in Eq. (2.17). More unexpected, though, is the observation that the much simpler liquid drop objects do not change their surface areas much, though, of course, this may be due to the chosen parameterisation.

Within dense suspensions, like blood, multiple fluid object interactions are likely. It is therefore appropriate to verify the stability of our cMCLBM method, in the context of complex, three-body interactions. Moreover, greater deformation levels in particular should be verified; the latter can be induced using three fluid object tests.

3.2.2 Three fluid objects

All data presented correspond to cuboid simulation box size $160 \times 100 \times 100$ on a D3Q19 lattice with periodic boundary conditions enforced between all faces. We choose to consider a representative subset of three fluid object interactions, viewed from the rest frame of a central fluid object, towards which two other, distinct fluid objects are propelled. The central object is expected to undergo a strong elongational straining motion, with the background fluid again shearing strongly in the contact region. We consider the symmetric process as follows (see Fig. 5).

We initialise the three objects such that there is no interface between them, off-setting two fluid objects in relation to the third, central, approximately stationary fluid object's centre of mass, by their radius. In this way, the interaction may be characterised by a single impact parameter. The two fluid objects ($Object_1$ and $Object_3$) "sandwiching" the central fluid object ($Object_2$) and are again propelled towards it, using a buoyancy force, with $Object_1$ ($Object_3$) being driven in the positive (negative) x-direction. It should be noted that no control was applied to the relative orientation of fluid objects, initially, in these tests. Of course, in the case of drops and spherical vesicles, no such control is
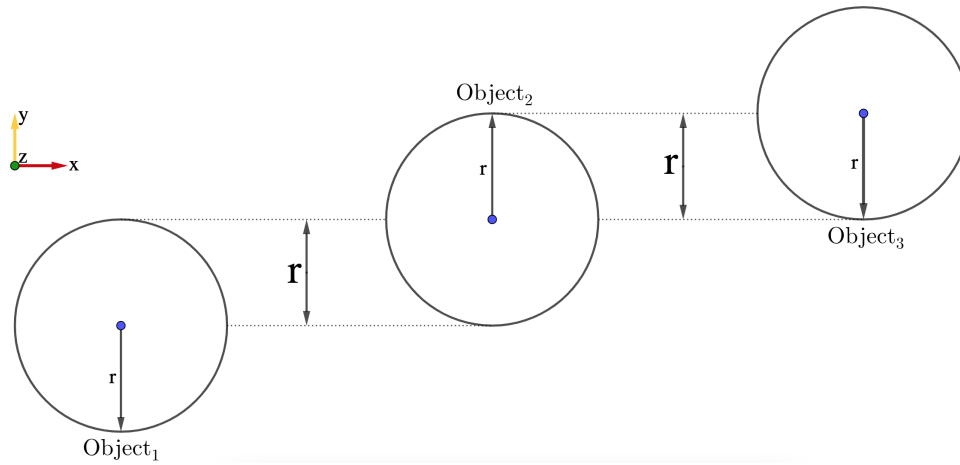
Figure 5: Schematic for the initialisation of a pseudo-ballistic impact test for three equivalent fluid objects. Two fluid objects (Object$_1$ and Object$_3$) are to be buoyancy-forced parallel to the x direction. Each of their centres is offset by an pseudo impact parameter, r, equal in value to the objects' initial radius, relative to a central, unforced fluid object (Object$_2$). Following initialisation, Object$_1$ (Object$_3$) is forced in the positive (negative) x-direction, generating a complex orbit about the central fluid object. Object 3 is expected to deform but to remain approximately at the centre of mass.

necessary. Note,the initial orientation of non-spherical erythrocytes, shown in Fig. 6(b) is arbitrary.

Figs. 6, show sequential orbit snapshots (A)-(D), taken from a pseudo-ballistic impact of three: liquid drops (a); erythrocytes (b); and three spherical vesicles (c). Fluid objects' interfaces are defined by the level set $\rho^N = 0$. The color density in these figures represents the surface area of the fluid objects. In all simulations, the applied buoyancy force for fluid Object$_1$ (Object$_3$) was $G = 1 \times 10^{-4} \hat{e}_x$ ($G = -1 \times 10^{-4} \hat{e}_x$) —see Fig. 5 for the objects' initial orientation.

From Figs. 6, we see that during the simulation of the liquid drops, the surface area of the drops now fluctuates, with a maximum relative fluctuation $\approx 33.6\%$. However, in the erythrocyte and spherical vesicle simulations, there is a much reduced membrane area fluctuation, of $\approx 1.5\%$ and $\approx 1.6\%$ respectively (across all objects in any one simulation). Table 4 gives numerical values. This result is of course expected by construction, both the erythrocyte and spherical vesicle should resist changes in membrane area. Accordingly, the most significant message conveyed by these data is that they provide verification of the effectiveness of our area-conserving force, outlined in [14], and defined in Eq. (2.17) above. The sandwiched drop however deforms significantly.

The data presented in this sub-section relate to fluid object interactions in the presence of shear flow in the contact region. Of course other classes of interaction, characterised by squeeze flows in the contact will occur in practice; (it is to the examination of these flows that we turn in the next sub-section). We also note that the maximum number of mutually immiscible fluids we have so far considered is four (three fluid objects and the background fluid). We have previously stated that, in three dimensions, stability

(a) Drops. 0, 7000, 14500 and 44500 time steps.

(b) Erythrocytes. 0, 7000, 15000 and 25000 time steps.

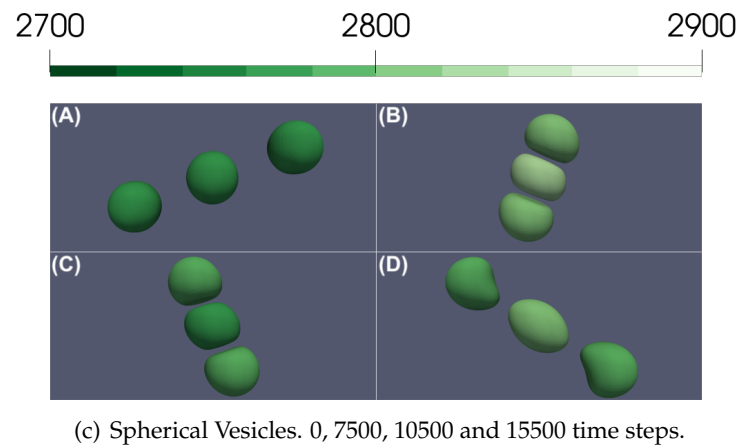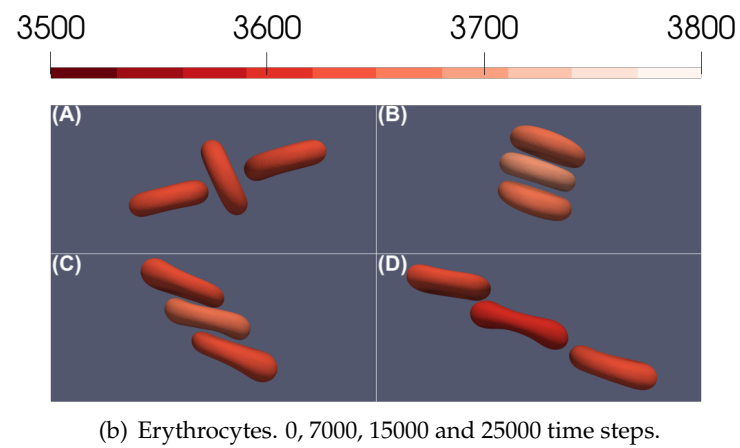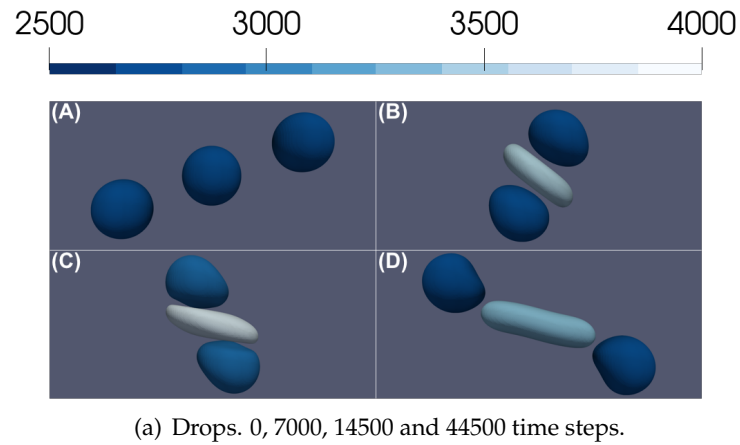(c) Spherical Vesicles. 0, 7500, 10500 and 15500 time steps.

Figure 6: A three fluid object pseudo-ballistic impact experiment, with sub-figures (a), (b), (c), corresponding to drops, erythrocytes and spherical vesicles, respectively. The system axes are as defined in Fig. 5, with snapshots viewed from a point on the positive z-axis. The bottom and top fluids objects were buoyancy forced in the positive (negative) x-direction, causing them to impinge on the central, unforced fluid objects. The indexed snapshots show the simulation time evolution in order (A)-(D) (given in sub-figure captions).

Table 4: Quantification of the maximum change in surface area, during the three object pseudo-ballistic impact tests for liquid drops, erythrocytes and spherical vesicles, shown in Figs. 6. This table shows the initial area of the fluid objects before the force was applied (Frame (A)), the maximum deviation of fluid object surface area, and then the relative maximum deviation for the fluid objects throughout the test.

	Initial Area	Max Deviation	Max Relative Deviation %
Drops	2762	3690	33.6
Erythrocytes	3633	3687	1.5
Spherical Vesicle	2771	2816	1.6

of a cMCLBM algorithm with five local fluids is necessary to underwrite applications containing unlimited numbers of fluid objects [44].
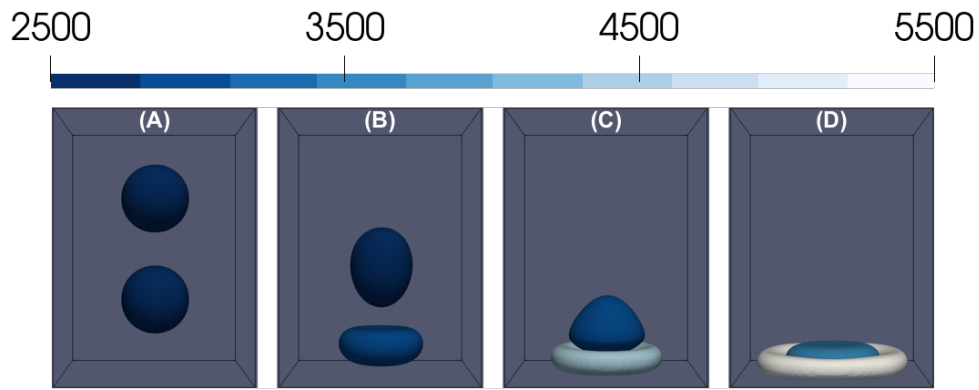
3.3   Two fluid object sedimentation

All data presented in this section derive from a cuboid simulation box of size $80 \times 80 \times 110$ using a D3Q19 lattice with no-slip boundary conditions, enforced by mid-link bounce-back imposed on all faces. Clearly, such a geometry will promote strong confinements effects.

Let us now consider orbits in which the background fluid motion in the contact is a squeeze flow, by sedimenting two fluid objects. Two fluid objects are initialised with their axes of rotational symmetry parallel to one another, separated by a distance such that there is no initial object-object interface. Once the objects have reached steady state shape, a buoyancy force of $G = -1 \times 10^{-4} \hat{e}_z$ is applied to both of the objects in the vertical direction. The objects then sediment towards the bottom of a simulation box enclosure, where they are forced to interact. The results from this test for multiple fluid objects are shown in Figs. 7. These data show the time evolution of the fluid objects in sequence (A)-(D) (time step counts and other parameters are case-specific and stated in the relevant figure caption); the color map corresponds to the fluid objects surface area.

These data represent a stringent test of the stability under flow stresses, amplified by confinement effects (the no-slip boundaries operate at the bottom of the domain). Data from Figs. 7, show all three simulation cases remained stable. As in the results in the ballistic impact tests, it can be seen that there is a much larger deformation of the liquid drops, in comparison to erythrocytes and spherical vesicles, for equivalent forcing and object size. For liquid drops, there is now a maximum relative fluctuation in surface area $\approx 94.1\%$, compared with $\approx 5.0\%$ and $\approx 7.7\%$, for the erythrocyte and vesicle, respectively, summarised in Table 5.

## 3.4   Four fluid object sedimentation

Finally, we consider the sedimentation of four fluid objects in a direct generalisation of the two fluid object test, considered in the previous subsection. All data presented in this subsection correspond to a cuboid simulation box size $75 \times 75 \times 250$ lattice units, on a

(a) Drops. 0, 7000, 14500 and 44500. time steps.
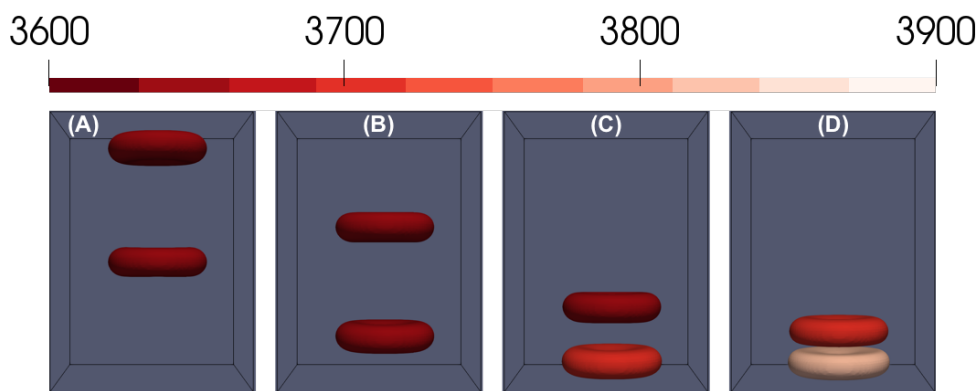
(b) Erythrocytes. 0, 20000, 40000 and 50000 time steps.
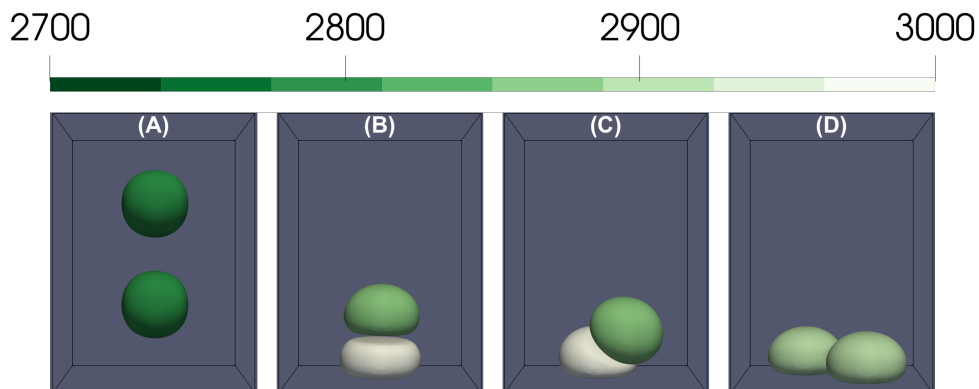
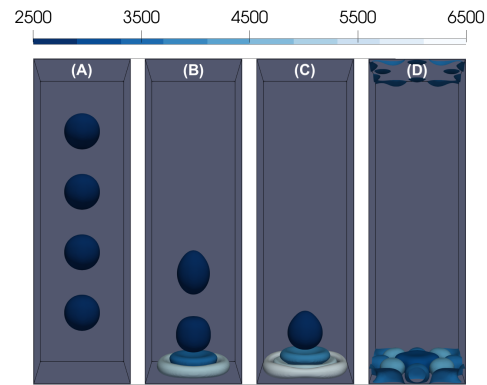(c) Spherical Vesicles. 0, 19500, 42000 and 97000 time steps.

Figure 7: Time evolution of two fluid objects in a sedimenting flow under confinement effects, with sub-figures (a), (b), (c), corresponding to drops, erythrocytes and spherical vesicles, respectively. The axes were orientated so that the x-y axes span the horizontal plane, and the z axis is orientated in the vertical direction. A buoyancy force was applied to all fluid objects in the negative z direction, with magnitude 0.0001 lattice units. The indexed snapshots show the simulation time evolution in order (A)-(D) (given in sub-figure captions).

Table 5: The maximum change in surface area during the two object sedimentation tests for liquid drops, erythrocytes and spherical vesicles, shown in Figs. 7. Columns parameterise the initial area of the fluid objects before the force was applied (Frame (A)), the maximum deviation of fluid object surface area during the test, and the relative maximum deviation for the fluid objects throughout the tests.

	Initial Area	Max Deviation	Max Relative Deviation %
Drops	2768	5374	94.1
Erythrocytes	3631	3812	5.0
Spherical Vesicle	2778	2993	7.7

D3Q19 lattice with no-slip boundary conditions, enforced by mid-link bounce-back imposed on all faces. Again, the fluid objects are initialised with their axes of rotational symmetry parallel to one another, separated by a distance such that there is no initial object-object interface. Once the objects have reached steady state shape, a buoyancy force of $G = -1 \times 10^{-4} \hat{e}_z$ is applied to all of the objects in the vertical direction. The objects then sediment towards the bottom of the enclosure, where they are forced to interact. Clearly, the dynamic contact flow and confinement effects must be expected to resemble those in the previous test, the key difference being that the compression force on the lowest fluid object in the stack will be increased. This test not only demonstrates the ability to simulate multiple fluid object interactions with our model, but also has considerable practical significance to the simulation of dense suspensions of fluid objects – the test demonstrates a five fluid simulation (the four fluid objects and the background fluids), which has been previously shown to correspond to the limiting number of independent fluids [44]. Put another way, it is established that, even when simulating extremely dense suspensions of fluid objects, one only needs to be concerned with the five fluids, with highest concentration at each lattice site (remaining fluid contributions being deemed insignificant).

The effect of the increased compression force due to the additional number of fluid object is very clear indeed in the drop data, from Fig. 8(a), when compared with data from the corresponding erythrocyte and spherical vesicle tests in Figs. 8(b) and 8(c). Indeed, we see that three out of the four liquid drops rupture, splitting into smaller drops, due to the increased compression force. Importantly however, the separate fluid species still remain immiscible with one another, highlighting the robustness of the extension to many immiscible fluids presented in Section 2.2. A comparison of the maximum change in cross-sectional area of the different fluid objects for this test, is shown in Table 6. Results confirm that, in the presence of the area conservation force, such as for the spherical vesicle and erythrocyte, the maximum change in cross-sectional area is much less than liquid drops with an extensible membrane. Ideally, we expect zero fluctuation for both the spherical vesicles and erythrocytes, however, due to the large flow stresses in this test and the inevitable presence of numerical error mainly in the constraint force, we see slight fluctuation in cross-sectional surface area. This is deemed as small, especially considering the fluid objects attempt to maintain shape throughout the test, as well as the large forces involved.

(a) Drops. 0, 29500, 42000 and 69500 time steps.
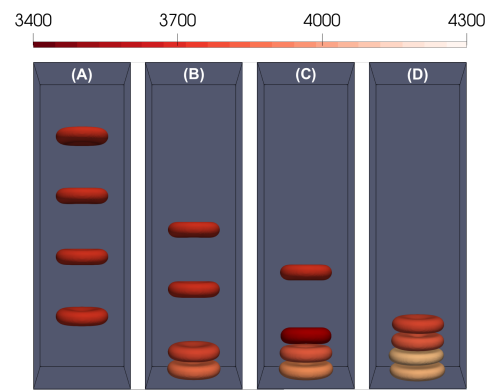
(b) Erythrocytes. 0, 50000, 85000 and 120000 time steps.
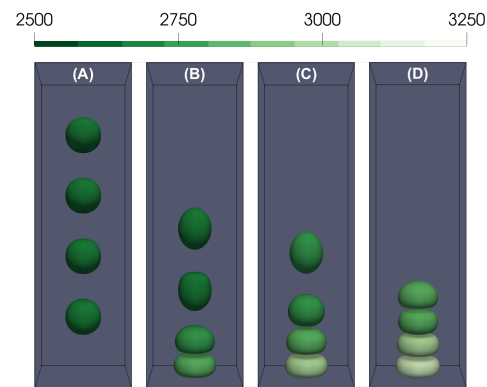
(c) Spherical Vesicles. 0, 19500, 24500 and 67000 time steps.

Figure 8: Time evolution of four fluid objects in a sedimenting flow under confinement effects, with sub-figures (a), (b), (c), corresponding to drops, erythrocytes and spherical vesicles, respectively. The axes were orientated so that the x-y axes span the horizontal plane, and the z axis is orientated in the vertical direction. A buoyancy force was applied to all fluid objects in the negative z direction, with magnitude 0.0001 lattice units. The indexed snapshots show the simulation time evolution in order (A)-(D) (given in sub-figure captions).

Table 6: Change in surface area during the four object sedimentation tests for liquid drops, erythrocytes and spherical vesicles, shown in Figs. 8. The initial area refers to the fluid objects before the force was applied (Frame (A)). The maximum deviation of fluid object surface area, and the relative maximum deviation apply to the entire test.

	Initial Area	Max Deviation	Max Relative Deviation %
Drops	2769	5624	103.1
Erythrocytes	3632	3921	8.0
Spherical Vesicle	2776	3089	11

4 Conclusion

We have confirmed in this work, the utility of an enhanced single framework cMCLBE method based upon the recent work of Spendlove et al. [14], here extended to three classes of fluid objects (spherical vesicles, erythrocytes and liquid drops), within the context of complex flows, induced in confined geometries, which constitute a searching test of simulation performance. Specifically, previously validated methodology [14] was extended in this work, to treat (i) a range of isolated fluid objects, characterised by different physical properties and (ii) multiple equivalent fluid objects. The resulting method involves complex immersed boundary forces (which we classify here) and therefore an obvious question arises regarding the integrity of fluid objects in fierce collisions- within cMCLBE, can one be confident that fluid objects' interfacial physics is preserved in the presence of potentially large local stain rates (viscous stresses) generated as multiple fluid objects interact? We deem the simplest way to answer this important question is to measure a defining property of the system – the fluid objects' interfacial area, A. Accordingly, the latter was taken as an accessible proxy for stability and physical veracity, for membrane area simply must be conserved in all interactions between vesicles, constraining even the most extreme deformation, whilst it can vary significantly when immiscible drops interact. Previous work has validated drop simulations [45]; accordingly we have emphasised vesicles here, but also provided data on equivalent drops tests, for context and to emphasise the ease with which a spectrum of fluid objects emerge from simple differential parameterisation of the method.

We might conclude from our reported series of tests, that the cross-sectional area of a vesicle membrane is a practical constant of the motion (but see below), verifying the algorithmic and computational integrity of the enhanced method (questions of quantitative validation of course remain). Put another way, A is confirmed to be almost constant, when measured along orbits of interacting vesicle objects whereas in equivalent drop simulations, A varies greatly. We note that even though only a finite number of flow geometries have been considered in this work, the simulated interactions encompass complex shear, squeeze and elongational-straining flows. Of course, some fluctuation in cross-sectional area is expected, even when simulating vesicles, due to numerical error arising from the discrete calculation of the vesicle's cross-sectional area and surface curvatures in simulation, and from the numerical implementation of the area constraint

force. As one might expect, the magnitude of observed fluctuations depends upon the magnitude of the shear and/or squeeze flow applied within the simulation. For instance, in the four erythrocyte sedimentation test, there was a larger fluctuation in cross-sectional area compared to the two erythrocyte pseudo-ballistic impact test, presumably due to the larger squeeze and compression forces exerted on the erythrocytes in the four fluid object case. However, we repeat that even though some level of error is expected in any numerical method, here manifest through the slight fluctuation of fluid object cross-sectional area, the fluid objects maintain their target shape, underscoring the effectiveness of the applied forces.

Procedurally, we have herein, treated up to five fluids (four fluid objects and background fluid). It has been shown previously [44] that algorithmic support for the simulation of five mutually immiscible species is sufficient to underwrite the efficient extension of the cMCLBE method to any number of mutually immiscible objects. To offset concerns regarding computational overhead, we remark here that the efficiency of the essential method applied to immiscible fluid objects will be considerably enhanced by proposed simplification of the definition of chromodynamic field, given in the appendix. We also note that a review of the computational cost and efficiency of the model is evidently needed, and is a legitimate concern for future work, where the impact of the proposed simplification of the definition of the chromodynamic field may also be assessed. Computational effort is not, of course, independent of: (i) the algorithm's physical veracity; (ii) the accuracy of the method; (iii) the convenience of the method; (iv) the level of software refinement.

In this work we have presented simulations characterised by the class of the fluid object; of course, there is no reason whatsoever to preclude mixing of object classes. Simulations containing poly-disperse populations of vesicles and drops straightforwardly fall within the scope of the method.

A Chromodynamic method for isolated fluid objects with improved computational efficiency

Currently, in cMCLBE, each fluid has an interface with every other fluid. When dealing with droplets, in the regime of completely arrested coalescence (where, by assumption, the surface of one drop will not wet another) and vesicles (which of course have no wetting interaction), this is an unnecessary expense —which will increase dramatically with the number of fluid objects. Therefore, a method to reduce the number of interfaces, through straightforward manipulation of the chromodynamic field definition, together with a commensurate modification to the segregation rule is a worthwhile step.

The currently accepted method for cMCLBM segregation is based of defining phase fields between each pair of fluids as follows:

$$C_i^{\psi\psi} = \frac{\rho_C}{\rho} f_i^{\psi} + \beta\omega_i \frac{\rho_C \rho_{C'}}{\rho} \underline{c}_i \cdot \hat{\underline{n}} + \beta\omega_i \frac{\rho_C \rho_{C''}}{\rho} \underline{c}_i \cdot \hat{\underline{n}} + \cdots, \tag{A.1}$$

where C, C' and C'' are three separate fluid species, C_i is the ith distribution of the fluid color C, and ψ ($\psi\psi$) is a post collision (post re-color) value. Now, for two particular fluids, say C and C', of equal density ρ, we straightforwardly obtain [15]:

$$\frac{2\rho_C(x)}{\rho} = (1+\tanh(\beta\mathbf{x})), \quad \frac{2\rho_{C'}(x)}{\rho} = (1-\tanh(\beta\mathbf{x})), \tag{A.2}$$

and so noting that the stable interface transect is well-approximated by the expression $\rho^N \approx \tanh(\beta\mathbf{x})$, we multiply the two equations together to obtain an approximate, algebraic expression for the color field:

$$\frac{4\rho_C\rho_{C'}}{\rho^2} = 1-\tanh^2(\beta\mathbf{x}) \approx \frac{1}{\beta}\nabla\rho_{CC'}^N, \tag{A.3}$$

where we have defined:

$$\rho_{CC'}^N = \frac{\rho_C-\rho_{C'}}{\rho_C+\rho_{C'}}, \quad C \neq C'. \tag{A.4}$$

We now substitute Eq. (A.3) into the segregation rule, Eq. (A.1):

$$C_i^{\psi\psi} = \frac{\rho_C}{\rho}f_i^\psi + \frac{\rho}{4}\omega_i\nabla\rho_{CC'}^N\underline{c}_i\cdot\hat{\underline{n}} + \frac{\rho}{4}\omega_i\nabla\rho_{CC''}^N\underline{c}_i\cdot\hat{\underline{n}} + \cdots. \tag{A.5}$$

Now, seeking to define only as many phase-fields as there are fluids, the traditional chromodynamic field between components C and C' is replaced as follows:

$$\rho_C^N \to \frac{\rho_C-\rho_{\overline{C}}}{\rho_C+\rho_{\overline{C}}}, \tag{A.6}$$

where we have defined:

$$(\rho-\rho_C) = \rho_{\overline{C}}. \tag{A.7}$$

Substituting the definition of $\rho_{\overline{C}}$ into our modified definition, we obtain a revised chromodynamic (phase) field as follows:

$$\rho_C^N = 2\frac{\rho_C}{\rho} - 1, \tag{A.8}$$

with a complementary segregation rule which has been adapted to only have a single dispersion term and a single segregation term:

$$C_i^{\psi\psi} = \frac{\rho_C}{\rho}f_i^\psi + \frac{\rho}{4}\omega_i\nabla\rho_C^N\underline{c}_i\cdot\hat{\underline{n}}. \tag{A.9}$$

Of course, it is important to verify that the new segregation is constrained by mass and momentum conservation, which is check by summing over i (directions) and all fluids, $C \in n$ (n is the number of nodal species).

$$\sum_i C_i^{\psi\psi} = \frac{\rho_C}{\rho}\sum_i f_i^\psi + \frac{\rho}{4}\nabla\rho_C^N\sum_i\omega_i\underline{c}_i = \rho_C, \tag{A.10}$$

as required, mass is conserved. Proceeding, we next sum the putative segregation over all fluids, $C \in n$:

$$\sum_{\forall C} C_i^{\psi\psi} = f_i^{\psi} \sum_{\forall C} \frac{\rho_C}{\rho} + \frac{\rho}{4} \omega_i \underline{c}_i \cdot \underline{v}, \tag{A.11}$$

where we have defined:

$$\underline{v} = \sum_{\forall C} \underline{\nabla} \rho_C^N = \underline{\nabla} \left(\rho_C^N + \rho_{C'}^N + \cdots + \rho_{C^n}^N \right), \tag{A.12}$$

where the n superscript in $\rho_{C^n}^N$, corresponds to the number of phase fields in the system, i.e., the number of nodal species.

Substituting the Eq. (A.8) into the above equation

$$\begin{aligned}
\underline{v} &= \underline{\nabla} \left(\frac{2\rho_C - \rho}{\rho} + \frac{2\rho_{C'} - \rho}{\rho} + \cdots + \frac{2\rho_{C^n} - \rho}{\rho} \right) \\
&= \underline{\nabla} \left(\frac{2(\rho_C + \rho_{C'} + \cdots + \rho_{C^n})}{\rho} - n \right) \\
&= \underline{\nabla} (2 - n) = 0, \tag{A.13}
\end{aligned}$$

again, where n is the number of nodal species, and is constant. Momentum may be shown to be conserved in like fashion.

Where a fixed number of fluids is tracked, the above simple re-definition has the potential to reduce the number of computations necessary at each node considerably.

References

[1] A. Farutin, T. Biben, and C. Misbah, 3D numerical simulations of vesicle and inextensible capsule dynamics, Journal of Computational Physics 275, 539–568 (2014).

[2] L. Landau and E. Lifshitz, Fluid Mechanics: Course of Theoretical Physics. Vol. 6, (1987).

[3] X. Dong, Z. Li, Z. Mao, and Y. Liu, Smoothed particle hydrodynamics simulation of liquid drop impinging hypoelastic surfaces, International Journal of Computational Methods 17, 1940001 (2020), https://doi.org/10.1142/S0219876219400012.

[4] C. Pozrikidis, Modeling and simulation of capsules and biological cells, 10 (2003), 10.1201/9780203503959.

[5] C. K. Aidun and J. R. Clausen, Lattice-Boltzmann method for complex flows, Annual Review of Fluid Mechanics 42, 439–472 (2010).

[6] R. M. MacMeccan, J. R. Clausen, G. P. Neitzel, and C. K. Aidun, Simulating deformable particle suspensions using a coupled lattice-Boltzmann and finite-element method, Journal of Fluid Mechanics 618, 13–39 (2009).

[7] T. Krüger, F. Varnik, and D. Raabe, Efficient and accurate simulations of deformable particles immersed in a fluid using a combined immersed boundary lattice Boltzmann finite element method, Computers & Mathematics with Applications 61, 3485–3505 (2011).

[8] C. S. Peskin, Flow patterns around heart valves: A digital computer method for solving the equations of motion, (1972).

[9] C. S. Peskin, The immersed boundary method, Acta Numerica 11, 479– 517 (2002).

[10] G. Závodszky, B. van Rooij, V. Azizi, and A. Hoekstra, Cellular level in-silico modeling of blood rheology with an improved material model for red blood cells, Frontiers in Physiology 8, 563–563 (2017).

[11] G. Zavodszky, B. van Rooij, V. Azizi, S. Alowayyed, and A. Hoekstra, Hemocell: A high-performance microscopic cellular library, Procedia Computer Science 108, 159–165 (2017).

[12] C. Armstrong and Y. Peng, Numerical simulations of capsule deformation using a dual time-stepping lattice Boltzmann method, Physical review. E 103, 023309–023309 (2021).

[13] B. Owen and T. Krüger, Numerical investigation of the formation and stability of homogeneous pairs of soft particles in inertial microfluidics, (2021), arXiv:2108.05277 [physics.flu-dyn].

[14] J. Spendlove, X. Xu, T. Schenkel, M. A. Seaton, I. Halliday, and J. P. Gunn, Three-dimensional single framework multicomponent lattice Boltzmann equation method for vesicle hydrodynamics, Physics of Fluids 33, 077110 (2021), https://doi.org/10.1063/5.0055535.

[15] K. Burgin, J. Spendlove, X. Xu, and I. Halliday, Kinematics of chromo-dynamic multicomponent lattice Boltzmann simulation with a large density contrast, Physical Review. E 100, 043310–043310 (2019).

[16] J. Spendlove, X. Xu, O. J. Halliday, T. Schenkel, and I. Halliday, Chromodynamic multirelaxation-time lattice Boltzmann scheme for fluids with density difference, Phys. Rev. E 102, 013309 (2020).

[17] J. Spendlove, X. Xu, T. Schenkel, M. Seaton, and I. Halliday, Chromo-dynamic multi-component lattice Boltzmann equation scheme for axial symmetry, Journal of Physics. A, Mathematical and Theoretical 53 (2020).

[18] T. J. Spencer, I. Halliday, and C. M. Care, Lattice Boltzmann equation method for multiple immiscible continuum fluids, Physical Review. E, Statistical, Nonlinear, and Soft Matter Physics 82, 066701–066701 (2010).

[19] Gunstensen, Rothman, Zaleski, and Zanetti, Lattice Boltzmann model of immiscible fluids, Physical Review. A, Atomic, Molecular, and Optical Physics 43, 4320–4327 (1991).

[20] A. K. Gunstensen and D. H. Rothman, Microscopic modeling of immiscible fluids in three dimensions by a lattice Boltzmann method, Europhysics Letters 18, 157–161 (1992).

[21] M. Latva-Kokko and D. H. Rothman, Static contact angle in lattice Boltzmann models of immiscible fluids, Phys. Rev. E 72, 046701 (2005).

[22] D. H. Rothman and J. M. Keller, Immiscible cellular-automaton fluids, J. Stat. Phys. 52, 1119 (1988).

[23] X. Shan and H. Chen, Lattice Boltzmann model for simulating flows with multiple phases and components, Physical Review E 47, 1815, 1819 (1993).

[24] Shan and Chen, Simulation of nonideal gases and liquid-gas phase transitions by the lattice Boltzmann equation, Physical Review. E, Statistical Physics, Plasmas, Fluids, and Related Interdisciplinary Topics 49, 2941–2948 (1994).

[25] M. R. Swift, W. R. Osborn, and J. M. Yeomans, Lattice Boltzmann simulation of non-ideal fluids, (1995).

[26] Swift, Orlandini, Osborn, and Yeomans, Lattice Boltzmann simulations of liquid-gas and binary fluid systems, Physical Review. E, Statistical Physics, Plasmas, Fluids, and Related Interdisciplinary Topics 54, 5041–5052 (1996).

[27] X. Li,, Z. Dong, Y. Li, L. Wang, X. Niu, H. Yamaguchi, D. Li, and P. Yu. (2022). A fractional-step lattice Boltzmann method for multiphase flows with complex interfacial behavior and large density contrast. International Journal of Multiphase Flow. 149. 103982.

10.1016/j.ijmultiphaseflow.2022.103982.

[28] P. J. Dellar, Nonhydrodynamic modes and a priori construction of shallow water lattice Boltzmann equations, Phys. Rev.E 65, 036309 (2002).

[29] X. Xu, K. Burgin, M. Ellis, and I. Halliday, Benchmarking of three-dimensional multicomponent lattice Boltzmann equation, (2017-11).

[30] Z. Guo, C. Zheng, and B. Shi, Discrete lattice effects on the forcing term in the lattice Boltzmann method, Phys. Rev. E 65, 046308 (2002).

[31] I. Halliday, X. Xu, and K. Burgin, Shear viscosity of a two-dimensional emulsion of drops using a multiple-relaxation-time-step lattice Boltzmann method, Phys. Rev. E 95, 023301 (2017).

[32] P. J. Dellar, Incompressible limits of lattice Boltzmann equations using multiple relaxation times, J Comput. Phys. 190, 351 (2003).

[33] X. He, S. Chen, and G. D. Doolen, A novel thermal model for the lattice Boltzmann method in incompressible limit, Journal of Computational Physics 146, 282–300 (1998).

[34] S. V. Lishchuk, C. M. Care, and I. Halliday, Lattice Boltzmann algorithm for surface tension with greatly reduced microcurrents, Phys. Rev.E 67, 036701 (2003).

[35] U. D'Ortona, D. Salin, M. Cieplak, R. B. Rybka, and J. R. Banavar, Phys. Rev.E 51, 3718 (1995).

[36] A. Guckenberger and S. Gekle, Theory and algorithms to compute helfrich bending forces: a review, Journal of Physics. Condensed Matter 29, 203001–203001 (2017).

[37] W. Helfrich, Elastic properties of lipid bilayers: Theory and possible experiments, Z. Naturforsch. C 28 (1973), 10.1515/znc-1973-11-1209.

[38] C. Trejo Soto, G. Lázaro, I. Pagonabarraga, and A. Hernández-Machado, Microfluidics Approach to the Mechanical Properties of Red Blood Cell Membrane and Their Effect on Blood Rheology, Membranes 12, 217 (2022).

[39] S. Leclaire, M. Reggio, and J.-Y. Trépanier, Progress and investigation on lattice Boltzmann modeling of multiple immiscible fluids or components with variable density and viscosity ratios, Journal of Computational Physics 246, 318–342 (2013).

[40] Y. Fu, S. Zhao, L. Bai, Y. Jin, and Y. Cheng, Numerical study of double emulsion formation in microchannels by a ternary lattice Boltzmann method, Chemical Engineering Science 146, 126–134 (2016).

[41] Y. Yu, H. Liu, D. Liang, and Y. Zhang, A versatile lattice Boltzmann model for immiscible ternary fluid flows, Physics of Fluids 31, 012108 (2019).

[42] G. Lester, Contact angles of liquids at deformable solid surfaces, Journal of Colloid Science 16, 315–326 (1961).

[43] J. S. Rowlinson and B. Widom, Molecular Theory of Capillarity (Clarendon Press, Oxford, 1982).

[44] M. Dupin, I. Halliday, C. M. Care, L. Alboul, and L. Munn, Modeling the flow of dense suspensions of deformable particles in three dimensions, Physical Review E 75, 066707 (2007).

[45] K. Burgin, Development of explicit and constitutive lattice-Boltzmann models for food product rheology, Ph.D. thesis, Sheffield Hallam University (2018).